Key Points:
- Evidence of submesoscale ageostrophic filaments and eddies in a western boundary current from HF radar, moored, and satellite observations
- Influence of the short-term wind variability on the surface currents, horizontal flow shear, frontal jet destabilization, and cyclonic eddy formation
- Contribution of coastal eddies and submesoscale fronts to the cross-shelf dispersion, advection, and mixing of productive shelf waters

Correspondence to:
A. Mantovanelli,
alessandra.mantovanelli@gmail.com

Lagrangian and Eulerian characterization of two counter-rotating submesoscale eddies in a western boundary current

Alessandra Mantovanelli[1,2] , Shane Keating[1] , Lucy R. Wyatt[2,3] , Moninya Roughan[1] , and Amandine Schaeffer[1]

[1]School of Mathematics and Statistics, University of New South Wales, Sydney, New South Wales, Australia, [2]College of Science, Technology and Engineering, James Cook University, Townsville, Queensland, Australia, [3]School of Mathematics and Statistics, University of Sheffield, Sheffield, UK

Abstract In recent decades, high-spatial resolution ocean radar and satellite imagery measurements have revealed a complex tangle of submesoscale filaments and eddies, in the surface velocity, temperature, and chlorophyll *a* fields. We use a suite of high-resolution data to characterize two counter-rotating, short-lived eddies formed at the front between the warm East Australian Current (EAC) and temperate coastal waters (30°S, Eastern Australia). In this region, submesoscale filaments and short-lived eddies are dynamically generated and decay at time scales of hours to days. Dominant cyclonic filaments of O(1) Rossby number formed along frontal jets and eddy boundaries, generating localized ageostrophic circulations at the submesoscale. Measurements of over-ocean wind direction and surface currents from high-frequency radars reveal the influence of the short-term, small-scale wind forcing on the surface circulation, enhancement of the horizontal shear, frontal jet destabilization, and the generation and decay of the cyclonic eddy. By contrast, the anticyclonic eddy formation was most likely associated with EAC mesoscale instability and anticyclonic vorticity. Lagrangian tracks show that surface particles can be temporarily trapped in the eddies and frontal convergent zones, limiting their transport. Mixing between EAC-derived and coastal waters was increased along the frontal regions, and particles starting at the divergent regions around the eddies experienced significant dispersion at submesoscales. The cyclonic cold-core eddy entrained high chlorophyll *a* shelf waters on its convergent side, suggesting spiral eddy cyclogenesis.

1. Introduction

In recent decades, high-resolution current measurements and remote sensing imagery have begun to unveil the surface dynamics of the ocean at kilometer scales. Sea-surface color images [*Pasquet et al.*, 2012; *Alpers et al.*, 2013] and observations of surface currents by ocean radars [*Roughan et al.*, 2005; *Parks et al.*, 2009; *Haza et al.*, 2010] and Lagrangian drifters [*Poulain et al.*, 2013; *Mantovanelli et al.*, 2012] reveal a complex tangle of eddies, fronts, and filaments on scales of 1–100 km [*Ferrari*, 2011]. These coherent flow structures have a significant impact on coastal patterns of transport and mixing, where they regulate biogeochemical fluxes and the dispersal of pollutants and organisms [*Lekien et al.*, 2005; *Baird et al.*, 2011; *Roughan et al.*, 2011].

Of particular interest are the dynamics of coastal eddies that form along western boundary currents because of their influence on biological productivity and fisheries [*Everett et al.*, 2011, 2015; *Mullaney and Suthers*, 2013]. Persistent eddies can isolate water masses for prolonged periods, aggregate or juxtapose populations of organisms, serve as reproduction refuges, and affect biological connectivity [*Owen*, 1981; *Largier*, 2003; *Roughan et al.*, 2011]. In addition, the cross-shelf transport of nutrients by coastal eddies can limit biological production in highly productive eastern boundary upwelling systems [*Gruber et al.*, 2011] or enhance productivity in typically oligotrophic western boundary currents [*Everett et al.*, 2015]. Less is known about the influence of short-lived submesoscale eddies on coastal productivity.

Here we analyze the evolution of two short-lived, submesoscale eddies in the East Australian Current (EAC) separation region, off Coffs Harbour (Eastern Australia, Figure 1a), and investigate the response of these eddies to spatiotemporal variability of the wind forcing. In this region, the continental shelf is narrow and the mesoscale circulation is dominated by the EAC, which flows poleward as a swift jet of warm waters along the slope with variable current speeds and volume transport [*Mata et al.*, 2000]. Intrusions of the EAC
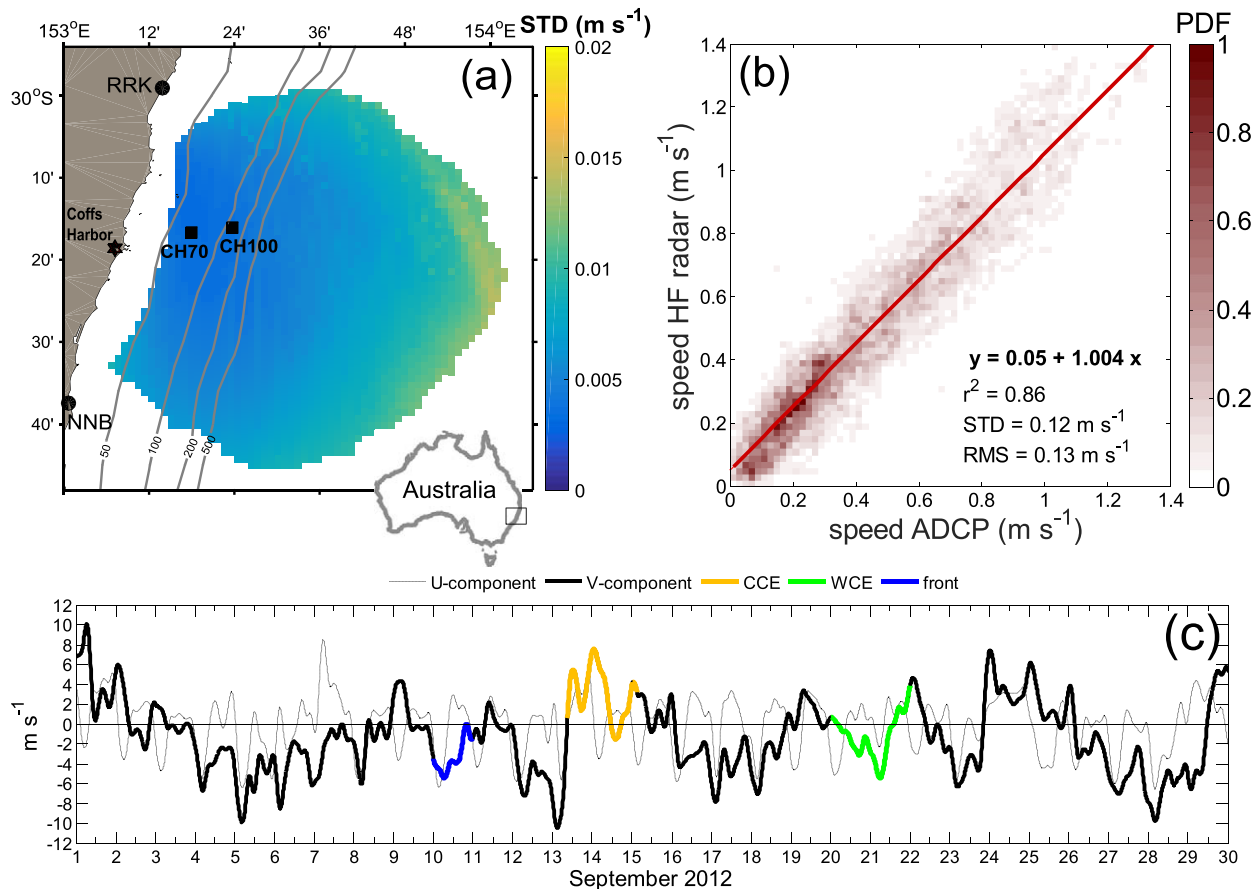
Figure 1. (a) HF radar domain offshore Coffs Harbour (Eastern Australia) with data coverage above 50% (September 2012 to September 2013) and locations of the radar stations (RRK, NNB; black circles), ADCP moorings (CH70 and CH100; black squares), and Coffs Harbour weather station (black star). Color legend shows the standard deviation (STD, m s^{-1}) of the v-component of the HF radar currents (6 h smoothed) calculated from the mean variance for September 2012 following methodology described in *Wyatt et al.* [2017]; (b) validation of surface HF radar currents against 10 m deep ADCP currents (6 h smoothed data; speed $= \sqrt{u^2 + v^2}$) at CH100 mooring shown by the linear regression (red line; equation in the figure; $p < 0.01$) and the joint probability density function normalized by its maximum value (PDF; color legend); (c) 6 h smoothed meridional (V-component, solid black line) and zonal (U-component, dotted black line) wind velocity components (m s^{-1}) measured at Coffs Harbour weather station (black star in Figure 1a) every 30 min; durations of the frontal jet (blue line), cold-core eddy (CCE; orange line), and warm-core eddy (WCE; green line) events are highlighted (see legend on the top).

near the coast generate thermal gradients and intensify the baroclinic flow [*Schaeffer et al.*, 2013, 2014a]. The local wind forcing has two main effects on the circulation in the region: south-westward blowing winds generate an offshore Ekman transport, coastal upwelling, and a poleward jet on the shelf; conversely, north-eastward blowing winds transport water onshore and favor downwelling and equatorward flow [*Middleton et al.*, 1997; *Schaeffer et al.*, 2013, 2014a; *Rossi et al.*, 2014].

In this study, we combine a suite of remote and in situ measurements (high-frequency radar surface currents and wind direction, temperature and current profiles and satellite imagery) to generate hypotheses about the formation and decay of two counter-rotating structures, one cold-core cyclonic eddy and one warm-core anticyclonic eddy. Radar-derived maps of over-ocean wind direction [*Wyatt*, 2012] show variability over short temporal and spatial scales and suggest the influence of the wind on the generation of horizontal surface shear flow and frontal destabilization. Both Eulerian (vorticity, divergence, and Rossby number) and Lagrangian (radar-based tracking and relative diffusivity of particles) approaches are applied to characterize the complex flow patterns and particle dispersion produced by the eddies.

In a related article, *Schaeffer et al.* [2017] present results from an automated eddy detection algorithm applied to radar surface currents from the same region over a 1 year period and show that cyclonic eddies are generated on average every 7 days, and anticyclonic eddies occur less frequently. The focus of *Schaeffer et al.* [2017] was on frontal eddies associated with meanders of the EAC that propagate at the inshore edge of the western boundary current over days or weeks independently of the wind stress. Most of the eddies

were short lived (life span < 2 days within the radar coverage) and a more detailed investigation on the role of the short-term wind-variability on their generation is required. This article investigates in detail the formation of two shorter-lived eddies from the same period, describing their evolution and response to wind variability using a variety of observational and analytical techniques, in order to highlight the hypothesis-generating power provided by combinations of data types.

The article proceeds as follows. In section 2, we describe the data and methodology used in this study. In section 3, we describe the influence of the short-term wind variability (hours to days) on the circulation of this region, before discussing in detail the evolution of two submesoscale eddies and their response to wind variability. In section 4, we discuss the Lagrangian properties and biological response of the eddies and hypothesize possible mechanisms responsible for their formation and decay. Section 5 summarizes our conclusions.

2. Data and Methods

2.1. HF Radar Measurements

A pair of land-based WERA phased-array high-frequency (HF) radars remotely measures surface currents in the top 0.9 m offshore Coffs Harbour (Eastern Australia, 30°S–31°S; Figure 1a). This HF system operates at 13.92 MHz frequency with radial and azimuthal resolutions of 1.5 km and 10.4°, respectively [*Wyatt et al.*, 2017]. Radial components (FV01 netcdf radial files; available at http://imos.aodn.org.au/imos) with intersection angles between 30° and 150° (good GDOP range), Bragg signal to noise larger than 10, and temporal coverage above 50% (over September 2012 to September 2013; Figure 1a) were averaged over a 30 min moving box and then combined to produce maps of the surface current field (u and v components) on a rectangular grid mesh with a spatial resolution of ∼1.5 km and a temporal resolution of 10 min [*Wyatt et al.*, 2017]. All times for radar measurements are in UTC.

At each grid point, absolute current velocity components larger than their annual averages plus 5 times their standard deviations or larger than 2.5 m s^{-1} were removed; the use of a Hampel filter (over three samples; five standard deviations) further improved the outlier removal. The u and v components were posteriorly smoothed over a 6 h window, using a polynomial (second degree) least square fitting Savitzky-Golay algorithm [*Savitzky and Golay*, 1964], and short temporal gaps (less than 1 h) were linearly interpolated. The Savitzky-Golay filter replaces each measurement with the constant term in the polynomial that is found by weighted (using the data variances) least squares fitting to the data points within the averaged time span. The variance of the constant term, and hence that of the smoothed current, is determined from the original variances through the least squares fitting procedure [*Wyatt et al.*, 2017]. Figure 1a shows the HF radar standard deviations after the 6 h smoothing for the v component of the flow, calculated as the square root of the averaged variances over September 2012; the errors for the u component were smaller and were not shown (more details on the HF radar error estimation are found in *Wyatt et al.* [2017]). The data smoothing further reduced data noise while retaining the short-time response of the flow to high-frequency winds on time scales of 7–27 h (Figure 2a).

Tidal currents represented only 2% (in average) of the flow variability over a 1 year period (September 2012 to September 2013) and could not be accurately separated from the wind-driven currents, which have strong diurnal and semidiurnal signals, and from inertial oscillations in the Coffs Harbour region. As a consequence, the data were not detided. Finally, surface current components were spatially averaged using an overlapping window to produce a 3 km spatial resolution.

2.1.1. Over-Ocean Wind Direction From HF Radar

Following the method of *Wyatt* [2012], the direction of the wind over the ocean was extracted from the two first-order Bragg peaks in the Doppler spectrum of the HF radar signal. These signals are backscattered from ocean waves with half the radar wavelength, one of which is propagating toward and the other away from the radar. These are short ocean waves that, except at very low wind speeds, are driven by the local wind. Wind directions are obtained from the relative amplitude of the two Bragg peaks from each of the two radars, applying a maximum likelihood fit of a hyperbolic secant function to the data at the cell of interest and the eight surrounding cells [*Wyatt et al.*, 1997; *Wyatt*, 2012]. This process is repeated for all cells with sufficient first-order signal to noise (> 10 dB), providing maps of hourly averaged wind direction (but not wind speed) with a 3 km spatial resolution over the radar domain. This procedure is implemented in a
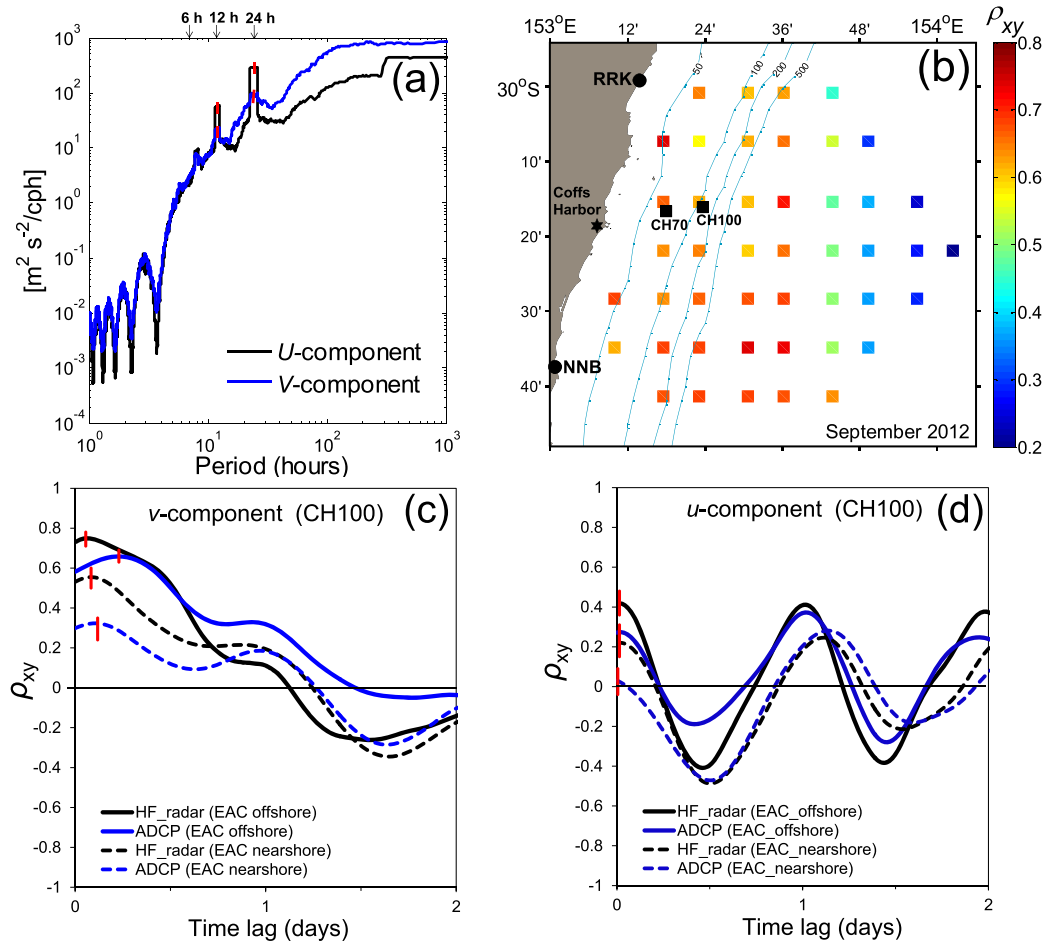
Figure 2. (a) Wind rotary spectra (September 2012 to September 2013) for *U*- and *V*-components (6 h smoothed data from Coffs Harbour weather station); red bars show the 95% confidence intervals using chi-square distribution with 62 degrees of freedom; the multitaper spectra [*Lilly*, 2016] were averaged in the frequency domain over 32 multiple Slepian tapers; the main peaks at 6, 12, and 24 h are highlighted on the top; (b) maximum cross-correlation coefficient (ρ_{xy}) between surface meridional currents (6 h smoothed data) and north-south ACCESS model wind velocity every 12 km during September 2012, showing the higher influence of the wind forcing on the surface circulation near the coast; (c) cross correlation (ρ_{xy}, cross-correlation coefficient) between 6 h smoothed surface meridional currents at CH100 mooring for HF radar (top 0.9 m) and ADCP (10 m depth) and north-south wind velocity (measured at Coffs Harbour station), see legend in the figure; the cross correlations are shown for two periods: (i) 1–19 September 2012 when the main EAC branch was offshore the radar domain (solid lines; EAC offshore) and the short-term surface circulation was mainly driven by winds and (ii) 20–30 September 2012 when the main EAC branch encroached upon the shore (dotted lines; EAC nearshore); cross-correlation coefficient and 95% confidence intervals were calculated following *Emery and Thomson* [2004] and *Bendat and Piersol* [2010]; (d) same as Figure 3c but for correlations between zonal currents and east-west winds.

software package provided by Seaview Sensing Ltd. *Wyatt* [2012] reports RMS differences between HF radar-derived and measured wind directions of 30°–50°; however, these measurements were not colocated.

Unit vectors were used to represent the HF radar wind field in the figures (i.e., Figures (3 and 4), and 8) because the method can only estimate wind direction, not wind speeds. The snapshot of wind direction with best spatial coverage measured 1–3 h before the HF currents was taken to allow for the lagged response of the surface flow (as shown in Figure 2c). A second data set was also used that provides both wind direction and intensity every 6 h with a 12 km spatial resolution obtained from the ACCESS numerical weather prediction model made available by the Australian Bureau of Meteorology (http://www.bom.gov.au/nwp/doc/access/NWPData.shtml). ACCESS data closest in time to HF radar observation were used in each plot. The time lags between the two data sets ranged between 0.5 and 2.5 h. ACCESS speeds in the text are given as mean values over the domain plus or minus the standard deviations. Linear correlations between ACCESS velocity data (closest to Coffs Harbour station; about 4 km away) and the land-based wind measurements produced r^2 of 0.8 and 0.5 for the *v* and *u* components, respectively.
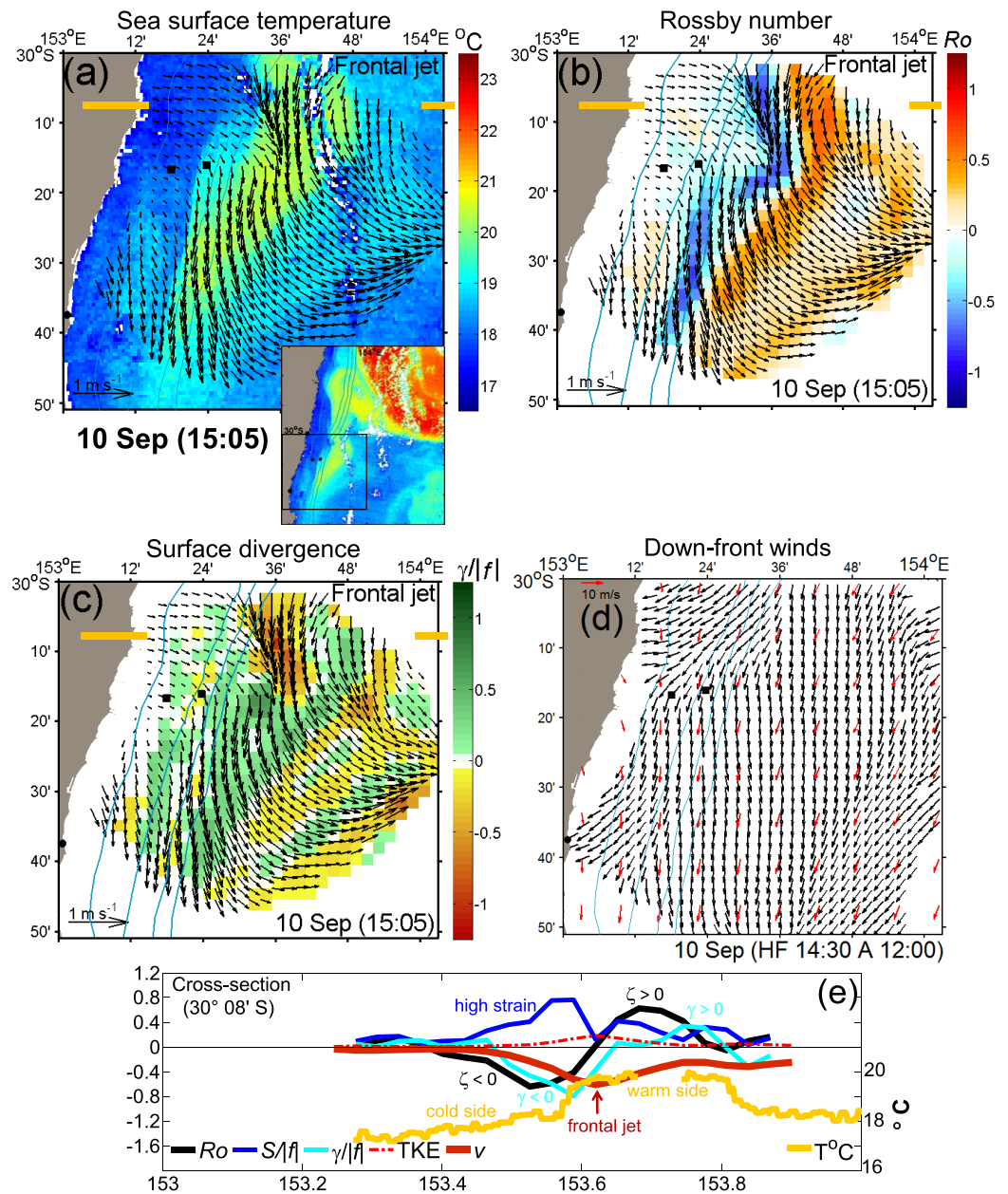
Figure 3. Warm frontal jet intruding Coffs Harbour region on 10 September 2012 visible on (a) sea surface temperature (°C, color legend) and surface HF currents (black arrows, m s^{-1}); (b) Rossby numbers ($Ro = \zeta/|f|$, color legend), darker blue and orange lines indicate cyclonic ($Ro < 0$) and anticyclonic filaments ($Ro > 0$), respectively; (c) surface divergence ($\gamma/|f|$, color legend), red ($\gamma/|f| < 0$) and green ($\gamma/|f| > 0$) tones indicate convergent and divergent regions, respectively; (d) HF radar wind direction (3 km resolution) using constant wind speeds for representation (black arrows) and 12 km resolution ACCESS model wind direction and intensity (m s^{-1}, red arrows; see speed scale on the top left); times for the HF radar and ACCESS wind snapshots are indicated by HF and A initials, respectively; (e) cross-self section on 30°08′S showing the opposite cyclonic (anticyclonic) vorticities on the cold (warm) sides of the jet; cross-section position is indicated by orange lines in Figures 3a–3c. Blue lines show the 50, 100, 200, and 500 m isobaths from land to ocean.

There are no other colocated measurements of over-ocean winds in the Coffs Harbour region taken at the same spatial and temporal resolutions of the HF radar observations. Comparison between wind direction measured by the radar (at the closest location to the Coffs Harbour weather station) and land-based directions gave a complex correlation coefficient of 0.52 and weighted average angular separation of 3.7. However, these two measurements were taken about 40 km away. Better agreement was found for comparisons between HF radar and ACCESS directions (September 2012 to September 2013), with complex correlation
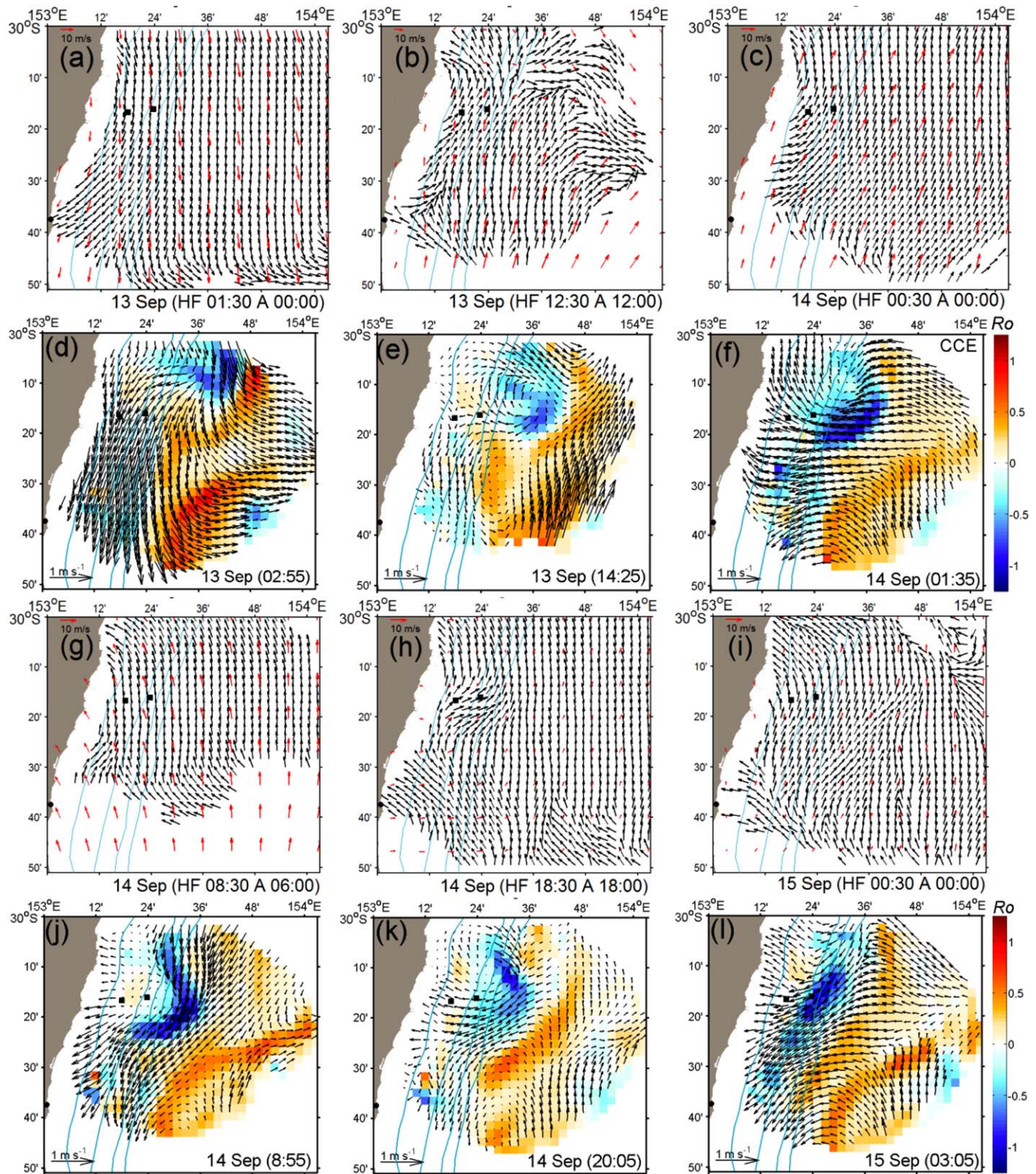
Figure 4. The CCE formation and decay; top plots (a–c and g–i) show HF radar wind direction (3 km resolution) using constant wind speeds for representation (black arrows) and the 12 km resolution access model wind direction and intensity (m s^{-1}, red arrows; see speed scale on the top left); and bottom plots (d–f and j–l) show the HF radar surface currents (m s^{-1}, black arrows) and Rossby number ($Ro = \zeta/|f|$, color legend); times for the HF radar and ACCESS wind snapshots are indicated by HF and A initials, respectively. (a) Strengthened southward winds; (b, c, g) winds reversed to north; (h, i) northward winds weakened; (d) northern dark blue region of strong cyclonic vorticity; (e) CCE started to form; (f, j) cyclonic ageostrophic circulation developed on the eastern flank of the CCE; (k) CCE started to decay; and (l) dissipated. Blue lines show the 50, 100, 200, and 500 m isobaths from land to ocean.

coefficients ranging from 0.63 to 0.81 in 70 locations within the domain. Averaged angular separations were less than $\pm 20°$ for 91% of the comparisons, and had a maximum absolute value of 38°. Overall the two data sets consistently represent the shifts between northward and southward wind directions, which are of interest for this work.

2.2. Overland Wind Measurements

Over-land wind data measured at Coffs Harbour (station number 59040 located at 30.31°S and 153.12° E) every 30 min were obtained from Australian Bureau of Meteorology. Wind speed is reported using the oceanographic convention (direction the wind blows to).

2.3. In Situ ADCP Current and Temperature Profiles

Current data profiles were measured every 5 min by two bottom-mounted ADCP (RDI Instruments, 307.2 kHz; bin size of 4 m) moored on the shelf (70 m isobath, CH70) and (100 m isobath, CH100; Figure 1a); thermistors installed on the moorings recorded water temperature every 8 m along the water column for depths below 10 m (more details in *Schaeffer et al.* [2013, 2014a, 2014b]). The ADCP data were corrected for magnetic declination, quality controlled to remove records contaminated by side-lobes and with low signal to noise ratio, and placed into uniform depth strata. Comparisons between the 6 h smoothed ADCP (at 10 m depth) and HF radar surface current speeds (September 2012 to September 2013) showed a good agreement for both CH70 and CH100 mooring locations ($r^2 \sim 0.6$–0.9; $p \sim 0$; RMS $\sim$ 0.1 m s^{-1}); the linear regression and joint probability distribution for the CH100 mooring comparison is shown in Figure 1b.

2.4. Satellite Images

We used MODIS AQUA level 2 images (resolution of $\sim$1 km) of sea-surface temperature (SST, °C) and chlorophyll a (mg m^{-3}, from OC4 algorithm; http://oceancolor.gsfc.nasa.gov) sampled daily or twice a day, projected to Mercator projection, and taken usually less than 10 min apart from the HF radar current measurements. The SST images served as a proxy for surface water density changes, which are mainly driven by the thermal gradients [*Schaeffer et al.*, 2014a, 2014b]. A total of 46 SST and 17 color images, available during September 2012, were used to identify daily variations on the extension of the EAC encroachment upon the shelf and of chlorophyll a spatial distribution, respectively.

2.5. Eulerian Diagnostics

Eulerian flow properties were calculated using centered differencing of the gridded surface current components (u, v) in the east-west (x) or north-south (y) directions, using the 3 km resolution and the 6 h smoothed HF radar data. The two-dimensional surface divergence, $\gamma = \frac{\partial u}{\partial x} + \frac{\partial v}{\partial y}$, implies vertical upwelling for divergent flows ($\gamma > 0$) or downwelling for convergent flows ($\gamma < 0$) by continuity. The local relative vorticity, $\zeta = \frac{\partial v}{\partial x} - \frac{\partial u}{\partial y}$, has anticlockwise ($\zeta > 0$, anticyclonic) and clockwise ($\zeta < 0$, cyclonic) rotations in the Southern Hemisphere. Both properties (γ, ζ) were divided by $|f|$ (Coriolis parameter) to facilitate comparison. The squared strain rate is given by $S^2 = (\frac{\partial u}{\partial x} - \frac{\partial v}{\partial y})^2 + (\frac{\partial v}{\partial x} + \frac{\partial u}{\partial y})^2$.

An uncertainty of the HF radar currents of 0.02 m s^{-1} (maximum error in Figure 1a) over three grid points (6 km) suggests that $\gamma/|f| < \pm$ 0.045 are indistinguishable from zero and were left blank in plots. The divergence of surface current velocities is a measure of vertical flux to/from the thin surface layer (top meter of the water column) sampled by the HF radar, which may result from upwelling, downwelling or vertical mixing [*Kaplan and Largier*, 2006].

The ratio $Ro = \zeta/|f|$ gives an estimate of the local Rossby number, keeping positive or negative values for anticyclonic or cyclonic rotations, respectively. The loss of geostrophic balance and generation of ageostrophic motions occur at large local Rossby numbers ($Ro \sim O(1)$), where the relative vorticity of the flow equals or exceeds the planetary vorticity, contrasting with typical $Ro \ll 1$ observed for mesoscale flows [*Mahadevan and Tandon*, 2006; *Thomas et al.*, 2008]. Localized flow regions with Ro of O(1) or larger are dynamically defined as submesoscale flows [*Thomas et al.*, 2008]. Submesoscale filaments typically form along fronts and at the edges of eddies through nonlinear instabilities of the mesoscale currents [*Gula et al.*, 2015]. Narrow lines of $Ro \geq 1$ are referred here as submesoscale filaments with strong ageostrophic circulation, and classified as cyclonic ($Ro \leq -1$) and anticyclonic ($Ro \geq 1$).

2.6. Lagrangian Analysis

The 2-D HF radar currents were inputted to a particle-tracking model to compute particle positions over time; the model uses bilinear interpolation of the velocity field on the 3 km resolution grid at each time step (10 min), an Euler Predictor-Corrector numerical method and projection of the tracked positions on the earth ellipsoid [*Mantovanelli and Heron*, 2012]; this model had an accuracy of ~4 km after 2 days of tracking when tested against surface drifters [*Mantovanelli et al.*, 2011]. Particles were released on a square grid with a grid spacing of 300 m in the HF radar domain and followed for 18 h. The relative dispersion (D^2) was calculated from the squared separation of the particle pairs, $D^2_{a,b}(t) = (x_a(t) - x_b(t))^2 + (y_a(t) - y_b(t))^2$, where the indexes ($a$, b) refer to each distinct particle in the pair. The relative diffusivity was calculated for each pair of trajectories as: $K_{R_{a,b}} = \frac{1}{4}\frac{d}{dt}D^2_{a,b}(t)$ [*Klocker et al.*, 2012].

3. Results

3.1. Wind Variability and Influence on the Surface Circulation

We analyzed a 1 year time series of wind speed recorded at the Coffs Harbour weather station (September 2012 to September 2013) to characterize the temporal variability of the wind. Multitaper rotary spectra [*Lilly*, 2016] detected two main peaks at the semidiurnal and diurnal signals but more pronounced in the *u* component of the wind velocity (Figure 2a). Analysis of the HF radar current spectra at Coffs Harbour mooring locations also showed diurnal and semidiurnal peaks both for surface (HF radar) and subsurface (ADCP) measurements [*Wyatt et al.*, 2017]. Wind varied in direction almost daily over the analyzed year, with a maximum persistence in each direction of less than 6 days (not shown).

Surface currents measured by HF radar represent a sum of geostrophic currents (mesoscale circulation), wind-driven ageostrophic currents (such as Ekman drift), tides, and other contributions [*Rio and Hernandez*, 2003; *Tokeshi et al.*, 2007]. Wind-driven currents near the surface are typically 1–4% of the wind speed at an angle of 0°–40° to the wind direction [*Ardhuin et al.*, 2009; *Chang et al.*, 2012]. We evaluated the short-term (hours to a couple of days) wind influence on the surface circulation using the lagged cross correlation between the wind and current velocity components [following *Emery and Thomson*, 2004]. In September 2012, maximum correlation coefficients (ρ_{xy}) between north-south winds given by the ACCESS model and meridional HF radar surface currents of 0.6–0.7 were observed nearshore and in the slope region, but the correlation decreased to a minimum of 0.2 at the farthest offshore site (Figure 2b); these results clearly show the higher influence of the wind forcing on the surface circulation near the coast during this period.

We also calculated the lagged cross correlations between the land-based winds (measured at the Coffs Harbour station) and both surface (HF radar data; top 0.9 m) and subsurface (ADCP data; 10 m depth) currents extracted at the CH70 and CH100 mooring locations (indicated in Figure 2b); results were similar at both locations and also similar whether or not land-based measurements or ACCESS wind data were used. Correlations between north-south winds and meridional currents are shown in Figure 2c and between east-west winds and zonal currents in Figure 2d. Based on the 47 sequential SST images, we split the data analyses in two periods: (i) 1–19 September, when the main EAC branch was offshore the radar domain (solid lines in Figures 2c and 2d; EAC offshore) and (ii) 20–30 September, when the main EAC branch encroached upon the shore (dotted lines in Figures 2c and 2d; EAC nearshore).

Correlation coefficients (ρ_{xy}) between meridional winds and north-south surface HF currents were ~0.75 under weak EAC influence (1–19 September) and reduced to ~0.55 as the EAC influence increases (20–30 September). Surface currents presented a time lag response to the wind forcing of 1–2 h. Similarly, meridional correlations for the ADCP currents dropped from ~0.66 (1–19 September) to ~0.32 (20–30 September) but subsurface currents had a slower response (~3–5 h; Figure 2c). Correlations between the east-west wind and current components were weaker ($\rho_{xy} < 0.4$) with a diurnal periodicity nevertheless they showed the same reduction pattern between the two periods (Figure 2d). All correlations were higher near surface (HF radar currents) than subsurface (ADCP currents). A higher contribution of the wind-induced circulation near the surface is expected, since the wind-driven Ekman currents decay exponentially with depth [*Graber et al.*, 1997].

These results clearly demonstrate that the importance of the wind forcing on the surface circulation increases at times and in regions less influenced by the mesoscale currents (EAC).

3.2. Relevance of Coherent Flow Structures (Eddies and Submesoscale Filaments)

Visual inspection of the HF radar surface currents (6 h smoothed, 3 km resolution), Rossby numbers, and SST images over 1 year period (September 2012 to September 2013) revealed that submesoscale filaments (3–30 km wide) often formed along the frontal jets and eddy boundaries associated with regions of high flow strain. The histogram of Rossby number for observations taken between September 2012 and September 2013 (25 million data points) shows that the distribution is notably skewed (skewness $= -1.38$), indicating the dominance of cyclonic filaments (areas with $Ro \leq -1$) which covered up to 30% of the radar domain (not shown).

Schaeffer et al. [2017] carried out a statistical study of the same region using an automated eddy-tracking algorithm and identified 40 cyclonic eddies over the period between September 2012 and September 2013. At least six of these features appeared to be frontal eddies propagating along the EAC, independently of the wind stress. Of the other structures, *Schaeffer et al.* [2017] found that the longest living eddies (up to 6 days under the radar coverage) were stalled by northward winds, while 34 other structures occurred during mean northward wind. Anticyclonic eddies occurred more rarely (16 in total over the analyzed year).

Here we address in detail the influence of wind forcing on two short-lived eddies, one cyclonic cold-core eddy (CCE) and one anticyclonic warm-core eddy (WCE) formed during September 2012. These eddies lasted ~2 days from the time the flow started meandering, forming a distinct circular or elongated vortex, until they dissipated. The eddies were formed in the presence of frontal jets (with thermal contrast of 2–5°C) and at times of high wind variability that increased the horizontal flow shear as described in section 3.2.1 (CCE) and section 3.2.2 (WCE).
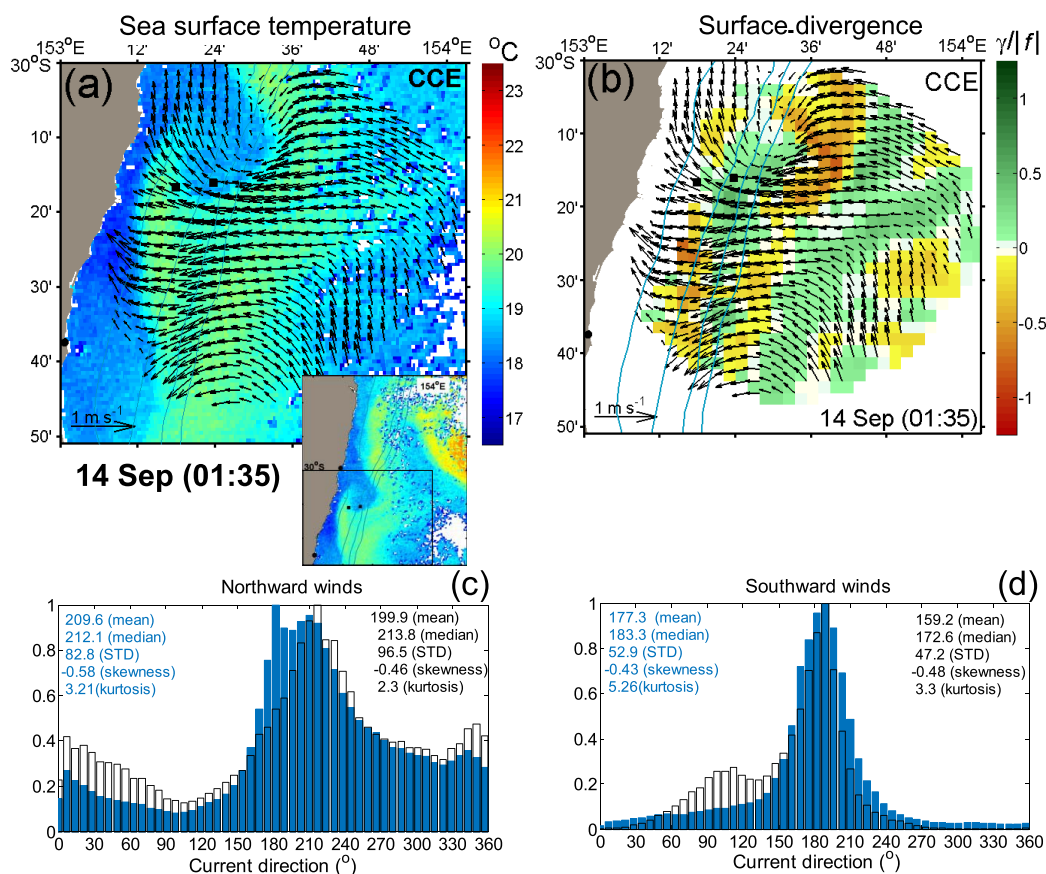

Figure 5. The cold-core eddy on 14 September 2012 visible on (a) sea surface temperature (°C; color legend) and surface HF currents (black arrows, m s^{-1}) and (b) surface divergence ($\gamma/|f|$, color legend); red ($\gamma/|f| < 0$) and green ($\gamma/|f| > 0$) tones indicate convergent and divergent regions, respectively. Histograms of the HF surface current direction normalized by the maximum count (values between 0 and 1) to facilitate comparison for days with (c) dominant northward winds opposing the frontal jet and (d) dominant southward winds favoring the frontal jet; black bars show the distribution during the frontal jet and CCE events and blue bars during the whole September 2012. Mean, median, standard deviation, skewness, and kurtosis values are shown in the figures for September 2012 (left side in blue) and the event days (right side in black).

3.2.1. Cyclonic Cold-Core Eddy (CCE)

We use SST images and HF radar maps of surface currents and wind direction between 10 and 15 September 2012 to illustrate the intrusion of a warm jet in the Coffs Harbour region, its interaction with shifting winds, and the development of a cyclonic cold-core eddy inshore of the jet (Figures 3–5). The frontal jet consisted of a tongue of mixed waters (SST ~19–21°C) that detached from the offshore EAC main jet (inset Figure 3a).

On 10 September, the jet was clearly visible as a 30 km wide warmer region (~19–21°C) of surface-intensified southward flow (speeds up to 0.6 m s^{-1} and kinetic energy up to 0.18 m^2 s^{-2}) contrasting the colder shelf waters (~16–18°C; Figures 3a, 3e, and 6a). Filaments (~3–9 km wide) of cyclonic (anticyclonic) relative vorticities developed on the west (east) sides of the jet axis (Figures 3b and 3e) associated with regions of high strain (S/|f| up to 0.8; Figure 3e). The surface flow was strongly convergent (γ/|f| up to −0.8) in the north portion of the jet (30°05′S–30°12′S; Figures 3c and 3e), indicating downwelling and the onset of frontogenesis. Southward winds were favoring the jet (Figure 1c) and HF radar/ACCESS wind maps show dominant, moderate (mean speed −5.6 ± 1.8 m s^{-1}) south-southwest winds within the domain (Figure 3d). *Thomas and Lee* [2005] pointed out that frontogenesis is strengthened by down-front winds, that is, winds blowing over a baroclinic zone in the direction of the surface currents.

On 11 September, radar/ACCESS data show weak (mean speed < |2.2| ± 2.3 m s^{-1}) winds with spatially variable intensity and directions within the domain (not shown), and the coastal weather station recorded a shift from southward to weakly northward winds (Figure 1c). At this stage, the frontal jet became unstable and meandered and surface currents flowed in opposing directions within different regions of the domain. On 12 September, winds rotated again toward south (Figure 1c) and the jet realigned with the alongshore direction.

On the beginning of 13 September, the southward winds strengthened considerably presenting approximately uniform direction and intensity over the whole domain (mean speed of −10.0 ± 2.8 m s^{-1} in Figure 4a) and resulted in a mostly southward flow (Figure 4d); the front weakened and Rossby numbers were overall reduced, except for a region of strong cyclonic vorticity in the north portion of the domain (Figure 4d).

On the second half of 13 September, a complex circulation pattern (Figure 4e, 14:25 UTC) developed as the winds reversed toward the north again (Figure 1c; mean speed of +7.0 ± 9.9 m s^{-1} in Figure 4b) and a cyclonic eddy formed in the northern portion of the domain (Figure 4e). Strong northward winds persisted
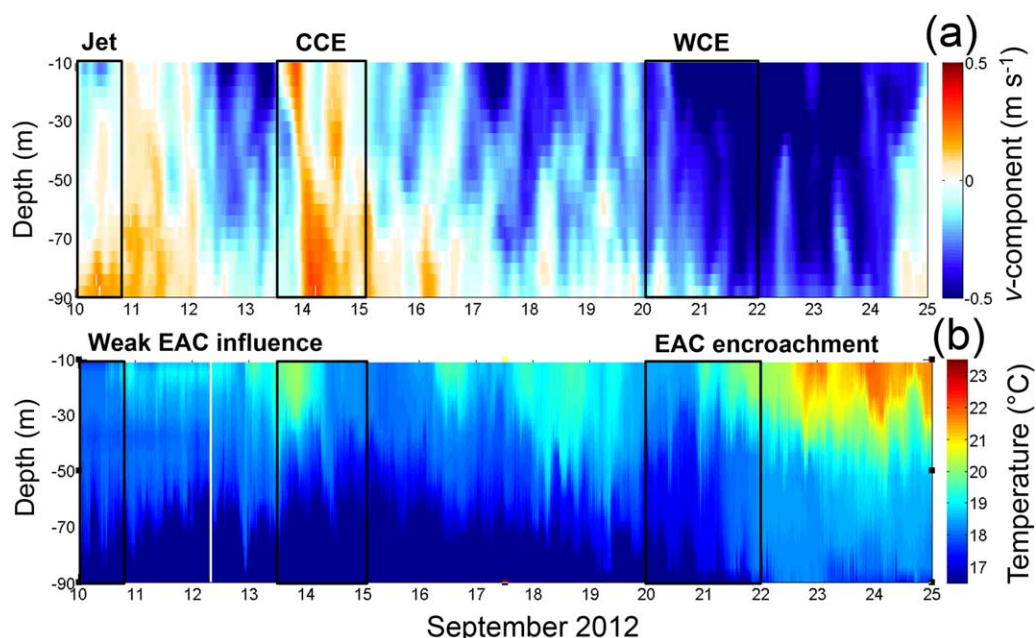

Figure 6. (a) The *v*-component of ADCP subsurface currents (below 10 m depth) and (b) temperature along the water column at CH100 mooring between 10 and 25 September 2012. Black rectangles indicate the life span of the frontal jet, CCE, and WCE.

until the first half of 14 September (mean speeds of $+7.9 \pm 1.9$ m s^{-1} in Figures 4c and 4g), generating intense onshore currents and submesoscale ageostrophic circulation ($Ro \sim -1$) on the eastern flank of the eddy subjected to high strain (Figure 4f). At this stage, colder coastal waters were entrained on the eddy core and the warm jet surrounded it (Figure 5a). Surface convergence dominated on the north-eastern flank and divergence on the south-western flank of the eddy (Figure 5b).

Profiles of water temperature and current speeds taken in the warm (CH70) and cold (CH100) sides of the frontal jet (south-west portion of the CCE) showed that: (i) the current reversed from southwest (before CCE) to northwest during the CCE formation (Figure 6a) and (ii) the temperature of the mixed layer (top 40 m) dropped by ~2°C on the cold side of the front (CH100; Figure 6b) and increased at the CH70 mooring as the warmer waters that surrounded the CCE reached it (not shown). The CCE decayed (Figures 4k and 4l) as the northward wind speeds decreased on 14–15 September (Figure 1c; mean speed of $+2.3 \pm 1.3$ m s^{-1} in Figures 4h and 4i).

Histograms of HF radar surface current direction are shown for periods (i) with northward winds opposing the frontal jet (Figure 5c) and (ii) southward winds favoring the frontal jet (Figure 5d) both during the frontal jet and CCE events (black bars in Figures 5c and 5d) and the whole month of September 2012 (blue bars in Figures 5c and 5d). Westward currents (240°–360°) were generated under northward winds (Figure 5c) while the surface flow was mainly restricted to the south direction (160°–200°) under southward winds (Figure 5d). These figures clearly show a higher variability of the current direction, i.e., 1.5–2.0 times higher standard deviation and 1.4–1.6 smaller kurtosis, under northward winds (opposing the frontal jet; Figure 5c) than under southward winds (favoring the frontal jet; Figure 5d).

3.2.2. Anticyclonic Warm-Core Eddy (WCE)

On 20–23 September 2012, the EAC approached the shore and its detachment region progressively migrated south (Figures 7a–7c). A WCE formed on 20–21 September (Figures 8d–8f and 8j–8k). During this period, weak northward winds (mean speed of $+2.2 \pm 1.7$ m s^{-1} in Figure 8a) shifted to southward with weak (mean speed of -2.5 ± 1.1 m s^{-1} in Figure 8b) to moderate speeds (mean speed of -6.5 ± 3.0 m s^{-1} in Figures 8c and 8g) and back to moderate northward winds (mean speed of $+6.0 \pm 1.7$ m s^{-1} in Figures 8h and 8i).

On day 21, the WCE was fully developed (diameter ~60 km; Figures 7b, 7e, and 8j) on the EAC branch that partially intruded on the radar area. An elongated tongue of cold water was visible between the EAC main jet and its branch (inset Figure 7b). A strong horizontal shear was observed between the southward flow (kinetic energy up to 0.25 m^2 s^{-2}) of cyclonic vorticity on the shelf (Ro up to -0.6), and the eastward turning EAC branch with anticyclonic vorticity (Ro up to 0.6; Figures 7g and 8j). Regions of surface divergence and convergence alternated within the domain (Figure 7e). A thermal contrast of ~5°C existed between the cold shelf waters and warm EAC branch (Figures 7b and 7g), with high strain ($S/|f|$ up to ~0.7) on the cold side of the front on the slope (Figure 7g). Both current profilers sampled within the frontal jet to show strong surface-intensified southward flows (e.g., CH100; Figure 6a) associated with warmer waters on the slope (CH100 mooring; Figure 6b) and ~2–3°C colder waters on the shelf (CH70 mooring; not shown).

On the second half of 21 September, the WCE migrated a few kilometers southwest and became elongated between the strong southward flow on the slope and the northward flow that intensified in open waters (Figure 8k) as winds rotated again to the north-northeast (mean speed of $+6.0 \pm 1.9$ m s^{-1} in Figure 8h). The eddy finally decayed on 22 September (Figure 8l) when a dominant onshore flow developed under dominant northward winds (Figure 8i). On 23 September, SST images show the encirclement of the cold tongue by the warmer waters (inset Figure 7c), as the EAC moved further south and encroached on the shelf under south-westward winds (Figure 1c).

4. Discussion

4.1. Influence on the Lagrangian Transport and Particle Dispersion

We demonstrated that coherent flow structures (such as submesoscale fronts and eddies) are formed and dissipate in the region offshore Coffs Harbour at time scales of hours to days in response to the combined influence of the EAC and wind forcing. Spatial and temporal variations of the wind direction and intensity and of the extent of the EAC encroachment upon the coast generate complex circulation patterns and the interaction between the frontal jet and winds can potentially aid the generation and dissipation of coastal
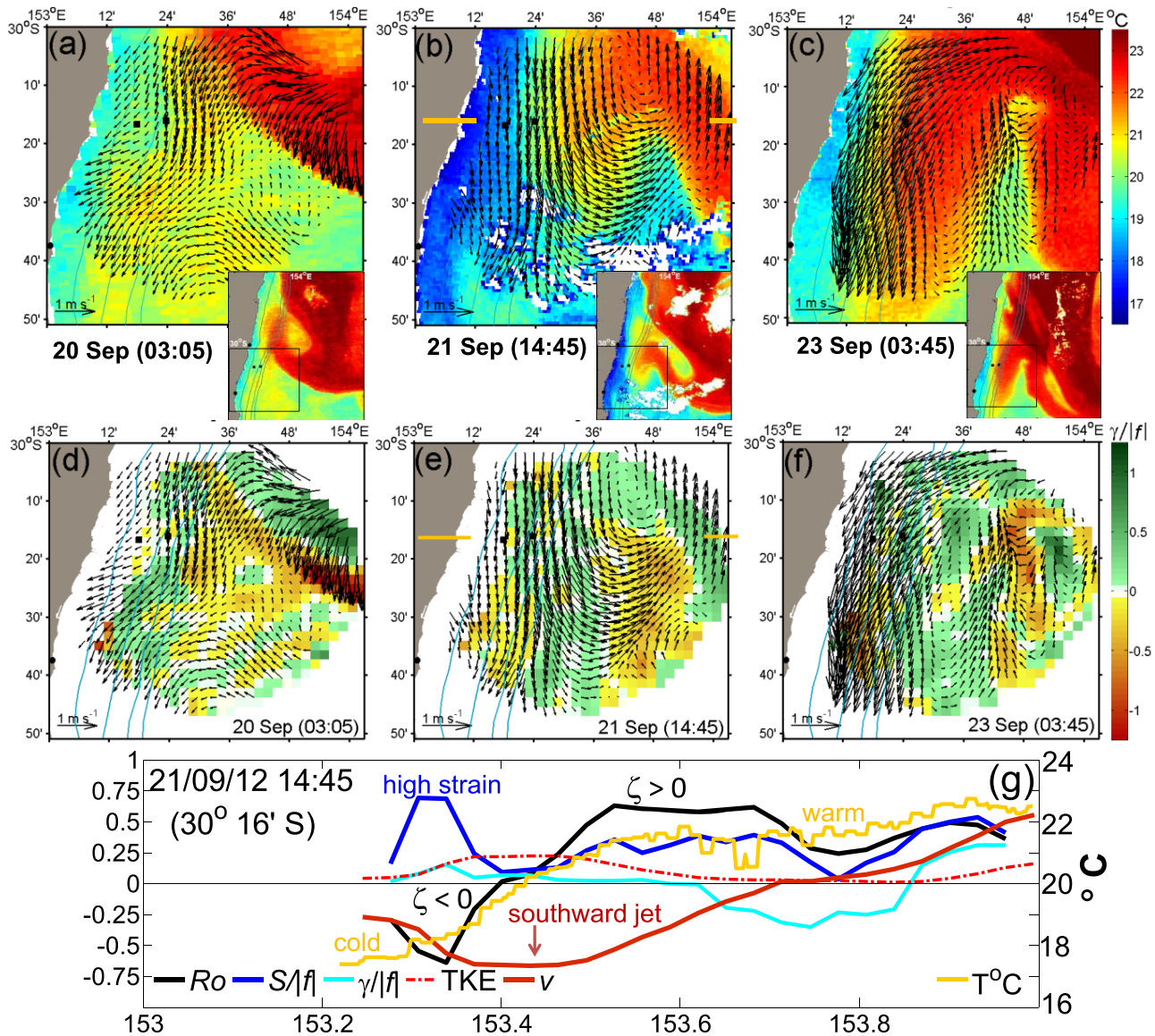
Figure 7. The warm-core eddy formation and decay; sea surface temperature (°C, color legend) and surface HF currents (m s⁻¹, black arrows) on (a) 20 September, (b) 21 September, and (c) 23 September; surface divergence ($\gamma/|f|$, color legend) on the (d) 20 September, (e) 21 September, and (f) 23 September; (g) cross section showing the strong cyclonic vorticity ($\zeta < 0$) on the cold side of the frontal jet and anticyclonic vorticity ($\zeta > 0$) on the warm side on 21 September (see also Figure 8j); cross-section position is indicated by orange lines in Figures 7b, 7e, and 8j.

eddies and submesoscale fronts. We applied the semiempirical Lagrangian tracking to evaluate the short-term influence of these coherent flow structures on surface transport and particle dispersion.

Lagrangian particle tracking showed that particles accumulated in zones of strong flow convergence formed along frontal regions (Figures 9a and 3c) as well as inside both the CCE (Figures 9b and 5b) and WCE (Figures 9c and 7e), and ∼26–36% of the particles had left the domain after 18 h of simulation. Particles traveled south and offshore with the frontal jet (Figure 9a). For the CCE particle tracking, a large number of particles were advected from the coast and concentrated in convergent regions inside and surrounding the eddy, with the remaining particles transported onshore or southward over the slope (Figure 9b). Particle advection by the WCE shows that particles released on the northwest portion of the domain were either advected southward by the strong frontal jet flow or offshore (Figure 9c).

The relative diffusivity (K_R) of a given particle pair depends on the particles' starting locations, pair orientation and time. Here pairs were formed between particles initially located at neighboring grid points in both
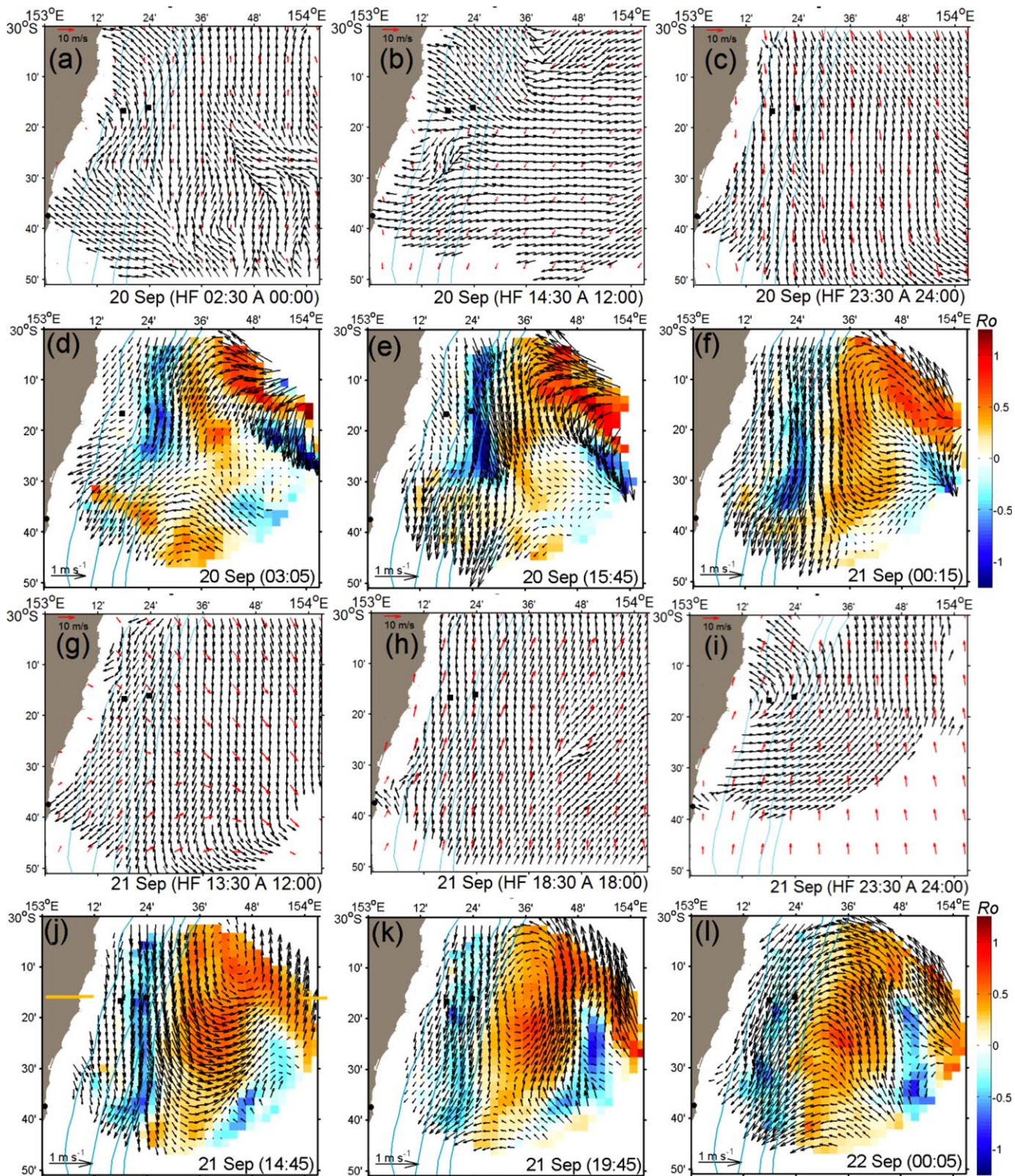
Figure 8. The WCE formation and decay; legend caption as for Figure 4. (a) Weak northward winds; (b) weak southward winds; (c, g) moderate southward winds; (h, i) moderate northward winds; (d, e, f) WCE developing; (j) WCE fully developed; (k) WCE stretched; (l) WCE dissipated.

the east-west and north-south directions. A sense of how the submesoscale eddies influenced the spatial pattern of particle dispersion can be obtained by plotting relative diffusivities K_R (after 18 h) at the starting location of the pair (Figures 9d–9f). Positive and negative values of K_R (averaged over initial pair
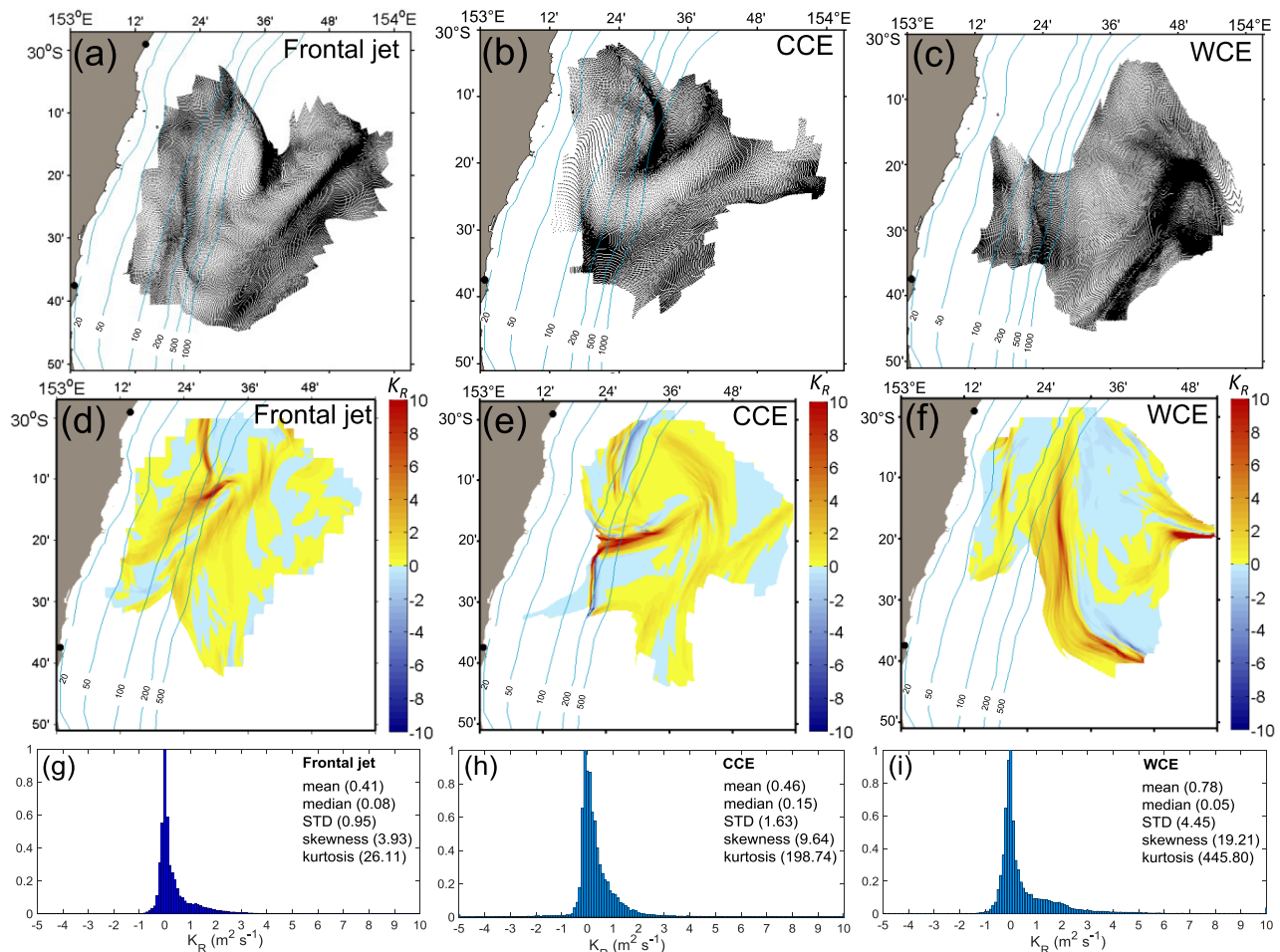
Figure 9. Snapshots of particle distribution after 18 h of simulation using the semiempirical particle-tracking model for (a) the frontal jet, (b) the cold-core eddy (CCE), and (c) the warm-core eddy (WCE). Mean relative diffusivities (K_R, m^2 s^{-1}; color legend) after 18 h, plotted at the initial particle position for the (d) the frontal jet, (e) CCE, and (f) WCE. Histograms of the mean relative diffusivities (K_R, m^2 s^{-1}) normalized by the maximum count (values between 0 and 1) to facilitate comparison for the (g) frontal jet, (h) CCE, and (i) WCE; y axis was restricted to -5 to $+10$ m^2 s^{-1} to facilitate visualization; maximum positive K_R values of 12, 53, and 137 m^2 s^{-1} were observed during the frontal jet, CCE, and WCE events, respectively.

orientations) indicate particle divergence and convergence, respectively. Relative diffusivities were low ($|K_R| < 1$ m^2 s^{-1}; Figures 9g–9i) within most of the domain, with alternating divergent ($K_R > 0$) and convergent ($K_R < 0$) regions.

The positive relativity diffusivities observed for the three events analyzed here (mostly below 5 m^2 s^{-1}; Figures 9g–9i) agree with the values estimated by *Nencioli et al.* [2013] for submesocale fronts; these authors found that 70% of the eddy diffusivity values ranged between 0.4 and 5 m^2 s^{-1}. Maximum positive K_R values of 12, 53, and 137 m^2 s^{-1} were estimated for the frontal jet, CCE, and WCE events, respectively. The WCE was more dispersive than the other two structures, with more instances of K_R above 1 m^2 s^{-1} (39%) than both the frontal jet and CCE (21–22%). This is likely due to the larger size of the anticyclonic eddy and the high kinetic energy of the frontal jet on its western boundary.

Narrow ridges of high positive diffusivity (i.e., $K_R > 1$ m^2 s^{-1}; red tones in Figures 9d–9f) occurred along both east and west frontal jet sides (Figure 9d), the south and east CCE flanks (Figure 9e), and the western WCE boundary (Figure 9f), which corresponded to starting locations of particles subjected to more intense spreading and dispersion. For instance, particle pairs released on the western flank of the WCE had larger relative diffusivity due to the separation of particles recirculating within the eddy, compared with those traveling consistently southward along the slope. By contrast, divergence on the southern flanks of the CCE increased the dispersion, mostly in the north-south direction but also in the across-shelf direction. This

highlights the importance of the submesoscale frontal regions and eddies for enhanced mixing and across-shelf dispersion.

Radar-derived convergent flows indicate locations where the surface mixed layer is thickening and the surface waters are being subducted [*Kaplan and Largier*, 2006]. Conversely, surface divergence indicates regions of flow separation where surface waters are replaced by water that upwells from below. In these Lagrangian simulations, virtual particles are advected by the surface currents only and cannot move in the vertical direction. However, the existence of convergent or divergent zones has important implications for real particle dispersion as surface particles accumulated in convergent fronts (red tones in Figures 3c, 5b, and 7e) could be potentially mixed downward. Conversely, upwelled water from divergent regions will be subjected to enhanced dispersion.

4.2. Biological Response

These three coherent flow structures (frontal jet, CCE and WCE) exerted an influence on the surface chlorophyll *a* distribution, as highlighted by 17 sequential ocean color images taken in September 2017. The frontal jet advected productive coastal waters southward from the EAC separation zone (∼29°S) up to the Coffs Harbour region (∼31°S; Figure 10a) over a period of 3 days; the cyclonic eddy entrained and transported shelf productive water offshore (Figure 10b) and the chlorophyll *a* concentrations were enhanced along the submesoscale fronts contrasting with the oligotrophic EAC waters (Figure 10c).

On 12 September (before the CCE formation), elevated chlorophyll *a* concentrations (above 2 mg m^{-3}) were restricted to the near-shelf region (onshore the 50 m isobath). This enhanced productivity was likely associated with coastal upwelling driven by strong southward winds on 12 September (Figure 1c), a typical phenomenon in the region [*Rossi et al.*, 2014]. At the time the CCE was formed, the productive shelf waters were entrained and advected ∼40 km offshore by the frontal jet, elevating the chlorophyll *a* concentrations inside the CCE (Figure 10b). This offshore advection is also seen in the Lagrangian simulations for particles starting offshore the 20 m isobath (Figures 9b and 10b). A zone of intermediate chlorophyll *a* is visible around the CCE boundary, likely resulting from the mixing of high chlorophyll *a* waters with the oligotrophic waters surrounding the eddy (Figure 10b). This is consistent with the overall increased dispersion (positive K_R) within the eddy and submesocale fronts (Figure 9e). Two days later, chlorophyll *a* concentrations were still high in the region previously occupied by the CCE.

However, chlorophyll *a* concentrations were much reduced (<0.3 mg m^{-3}) over the HF radar domain in the next available image on 20 September (start of the WCE formation), as the oligotrophic EAC waters encroached on the shelf. Unfortunately, no ocean color imagery was available for the WCE, but it was unlikely to have elicited as strong a biological response as that of the CCE since the 23 September satellite image (Figure 10c) also shows oligotrophic waters near the coast except for relatively higher chlorophyll *a*
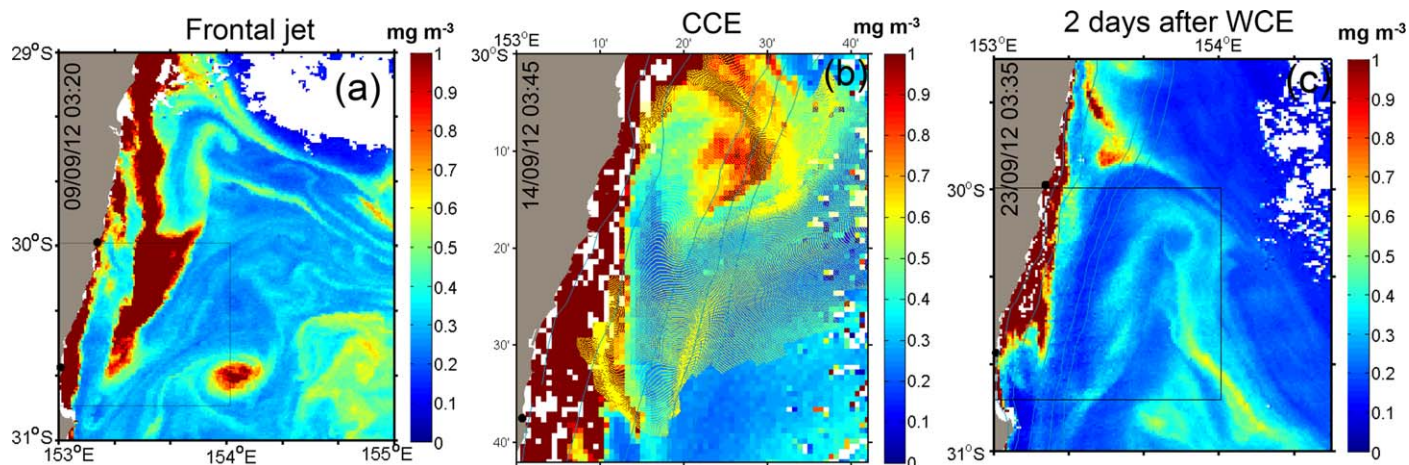

Figure 10. (a) Chlorophyll *a* from MODIS image on 9 September (03:20 UTC) showing the southward advection of high chlorophyll *a* waters within the frontal jet; (b) the offshore entrainment of productive shelf waters by the cyclonic eddy on 14 September (03:45 UTC) with final particles position (yellow dots) after 18 h of tracking on top; (c) oligotrophic EAC waters on the shelf 2 days after the WCE (23 September, 03:35 UTC) but enhanced chlorophyll *a* concentrations along the submesoscale fronts. Black square shows the HF radar domain and black dots the HF radar stations.

concentrations ($\sim$0.4–0.6 mg m^{-3}) associated with the submesoscale cold filaments (Figure 7c). Submesoscale filaments can generate localized areas with strong ageostrophic circulations and vertical motions (O(100) m d^{-1}), playing an important role in local mixing and productivity [*Lévy et al.*, 2012].

The interaction of eddies with a shelf-break current may account for a substantial portion of net cross-frontal exchange [*Cenedese et al.*, 2013]. The two short-lived frontal eddies observed here could potentially facilitate the across-shelf exchange of marine organisms (such as larvae and eggs) between shelf and oceanic waters. The CCE promoted the offshore movement of nutrient-rich shelf waters and the inshore movement of warmer EAC waters as well as temporarily trapped particles within the eddy and convergent frontal regions, limiting their southward advection. The WCE advected shelf waters offshore, increasing the across-shelf dispersion of a number of particles (and potentially marine organisms) initially located near the shelf, which are eventually reabsorbed by the EAC main jet and transported southward.

In a related paper, *Schaeffer et al.* [2017] show that small-scale frontal eddies form regularly in this region. Recently, *Roughan et al.* [2017] extensively sampled a similar cyclonic frontal eddy in the same region and found that the eddy was considerably more productive and had a higher proportion of coastal larval fish species than the surrounding waters. These studies and the results presented here suggest that short-lived submesoscale eddies may play an important role in productivity along the coast of south-eastern Australia.

4.3. Processes Controlling Submesoscale Eddy Formation and Decay

Previous studies have shown the influence of wind for the generation of both: (i) highly nonlinear cyclonic eddies ($|Ro| > 1$) linked to a wind burst event [*Alpers et al.*, 2013] and (ii) anticyclonic eddies associated with baroclinic instabilities of growing flow meanders set up by shifts in the wind direction [*Hansen et al.*, 2010] or bathymetric constraint of a wind-driven barotropic flow [*Schaeffer et al.*, 2011].

The high-resolution radar-derived maps of wind direction used in this study permit a more detailed analysis of the role of spatial variation of wind direction on the formation, evolution, and decay of submesoscale eddies. We emphasize that, in the absence of a full, time-dependent, three-dimensional picture of the flow within the domain, such an analysis will necessarily be speculative. However, the dynamical scenarios discussed in this section are consistent with the radar-derived measurements of surface currents and wind direction. Moreover, the analysis demonstrates the potential of combinations of observational and analytical techniques to generate hypotheses about the driving processes in these ephemeral, highly dynamic flow features.

4.3.1. Cyclonic Cold-Core Eddy (CCE)

A plausible mechanism for the generation of the short-lived cyclonic eddy described here was instability of the surface frontal jet accelerated by northward winds. Although the intruded frontal jet originally had a cyclonic relative vorticity (Figure 4d; northern portion), the jet deflection toward the shore was boosted by the onshore flow (Figure 4f) generated under strong northward winds (Figure 4c). This increased the horizontal velocity shear and, at the same time, stretched the meandering front, elevated the strain, and resulted in localized submesoscale ageostrophic circulation on the eddy's eastern boundary (Figures 4f and 4j). Cyclonic (anticyclonic) relative vorticities occurred on the cold inshore (warm, offshore) sides of the meandering frontal jet (Figures 4f and 4j).

The CCE formation is consistent with theoretical models of spiral eddy cyclogenesis. The spiral eddy originates from an ageostrophic frontal preconditioning phase with strong cyclonic shear on one side of the front and weak anticyclonic shear on the other side, followed by shear (barotropic) instability that winds up the front [*Munk et al.*, 2000] or baroclinic instability associated with frontogenesis on streaks of strong cyclonic shear and convergence [*Eldevik and Dysthe*, 2002].

Our hypothesis is that wind stress opposing the frontal jet can promote and/or accelerate frontal destabilization at short timeframes (hours to days) and submesoscale spatial scales, aiding the generation of coastal cyclonic eddies. In the Coffs Harbour region, the frontal jet flows predominantly southward and the opposing northward winds can potentially destabilize the jet while southward winds strengthen it (as suggested in Figures 3–5). This pattern is apparent in histograms of the surface current direction under northward and southward winds (Figures 5c and 5d). The distribution of surface current direction under northward winds shows greater variability while the distribution of surface current direction under southward winds is largely

confined to a narrow band. This suggests that interactions between the wind and frontal jet can increase the spatial variability of surface currents and generate complex circulation patterns.

Winds were mostly northward during the CCE formation with speeds of up to 8–11.1 m s^{-1} (Figure 1c; orange line and maximum speed in Figures 4b, 4c, and 4g), this could potentially generate wind-driven currents of the order of 0.3–0.45 m s^{-1} (assumed 4% of the wind speed) [*Ardhuin et al.*, 2009; *Chang et al.*, 2012] deflected to the left (northward/onshore) of the wind direction. The northward currents opposed the southward jet (speeds ∼0.3 to 0.6 m s^{-1}; Figure 6a on September 13) and deflected the jet onshore. However, the eddy started to decay as the wind intensity decreased (Figures 4h and 4i) and the southward jet flow dominated again (Figures 4k and 4l, end of September 14 and 15). The entire scenario is more complex because both wind direction and the EAC influence vary spatially and temporally.

4.3.2. Anticyclonic Warm-Core Eddy (WCE)

Several factors could have contributed to the formation and decay of the anticyclonic warm-core eddy, including the presence of submesoscale ageostrophic circulations, mesoscale baroclinic instabilities of the growing EAC jet meander, and to some extent the high variability of the wind direction. A higher across-shelf thermal contrast (∼5°C) was observed between the cold shelf and the warm EAC waters during the formation of the WCE (Figure 7b). Relative vorticities of opposite sign occurred on either side of the energetic southward flowing frontal jet, with high cyclonic vorticity on the cold side of the frontal jet and anticyclonic vorticity on the warm side (Figures 7g and 8j). *Macdonald et al.* [2013] showed that a mesoscale WCE started in a state of disequilibrium with a higher cyclonic vorticity ring outside at the density front between the EAC and the eddy and that the eddy grew by transfer of vorticity and mass from the EAC into the eddy.

Another possible generation mechanism for the WCE is associated with mesoscale instabilities of the EAC jet. A growing, wave-like distortion of the EAC jet was observed during the formation of the WCE, leading to the intrusion of a colder tongue between two EAC warm branches (inset Figure 7b). A slantwise exchange of cold and warm waters is often generated across a heavily meandering jet, which eventually pinch off to form eddies when meanders amplify [*Williams and Follows*, 2011]. Frontal wave growth can result from different processes, such as baroclinic instability [*Barth*, 1989, 1994], combined local baroclinic/barotropic instabilities [*Lozier et al.*, 2002] and interactions of an unstable jet with the coastline and bottom topography [*Witter and Chelton*, 1998; *Lozier and Reed*, 2005].

The wind stress during the WCE formation was predominantly southward (70% of the time) and weaker than that observed during the CCE (Figure 1c, green line and mean speed between +2.2 and −7.2 m s^{-1} in Figures 8a–8c and 8g). Therefore, it is unlikely that the frictional forcing induced by the wind alone could explain the current vorticity, and the EAC anticyclonic vorticity was most likely the primary driver for the WCE formation. The wind influence was more evident during the WCE decay (toward the end of 21 September), as the eddy was stretched between the southward flow on the shelf and the northward flow generated offshore (Figure 8k) when the winds rotated toward north (mean speeds of 6.0 ± 2.0 m s^{-1} in Figure 8h). The eddy subsequently dissipated as moderate northward winds persisted (Figure 8i), generating a mostly onshore flow (Figure 8l).

5. Conclusions

We used a suite of high-resolution measurements to analyze the formation and decay of two counter-rotating submesoscale eddies (one cyclonic cold-core eddy and one anticyclonic warm-core eddy) in the East Australian Current separation zone and to generate hypotheses about the mechanisms controlling their dynamics. Spatial maps of over-ocean HF radar wind direction provided insight into the short-term, small-scale wind influence on the frontal jet and eddy dynamics. The analysis of the Eulerian flow properties and Lagrangian particle dynamics depicted the structure of the frontal eddies and show the influence of the eddies on surface transport and particle dispersion.

The near-surface circulation changed over small spatial scales (a few kilometers) and short time scales (hours to days) due to the combined effect of the ageostrophic wind-driven flow and the mesoscale EAC current. The intensity and direction of the resultant surface flow was shown to depend on the relative strength and direction of these two flow components. The wind-driven currents are likely to be stronger either inshore or offshore of the frontal jet where they encounter less resistance from the opposing flow that increases the horizontal flow shear.

We hypothesize here that northward winds opposing the frontal jet aided the frontal jet meandering and the generation of the short-lived cyclonic eddy (Figures 4 and 5). By contrast, the warm-core eddy (Figures 7 and 8) formed under relatively weaker, southward winds and it is unlikely that the frictional forcing induced by the wind alone could explain the current vorticity; the EAC anticyclonic vorticity and its mesoscale instability most likely drove the warm-core eddy formation while winds aided the eddy dissipation. Our observations suggest that complex interactions between the frontal jet and winds near the coast are important for the understanding of the dynamics of submesoscale fronts and eddies in the EAC separation region.

Lagrangian particle tracking and relative diffusivities show that a large number of particles can be temporarily trapped at convergent fronts and within the core of eddies, limiting their transport to other areas. However, some particles starting in the divergent zones around the eddies experience strong dispersion at the submesoscale. Mixing between EAC-derived and coastal waters was increased along the submesoscale fronts, and satellite images suggest increased chlorophyll a concentrations in these locations. The frontal jet advected productive shelf waters southward along the shelf and the CCE entrained biologically rich shelf waters, elevating chlorophyll a concentrations on the slope and offshore regions, which were mixed with the oligotrophic EAC waters. Thus, short-lived coastal eddies and fronts may play an important role in the across-shelf transport of properties and marine organisms and mixing.

This paper demonstrates the power of and the need for the combination of high-resolution data from multiple platforms (such as HF radar, satellite images, and ADCP) to analyze the dynamics of submesocale eddies and fronts with short life span (hours to days) in western boundary currents systems. In addition to their power in generating and testing hypotheses about coastal ocean dynamics, data combinations such as those discussed here are useful for informing multi-platform sampling strategies; for indicating where the present technology, sensors and data products are lacking; and for providing impetuous for the improvement of high-resolution models. In particular, the lack of high spatial and temporal resolution wind velocity data over the ocean prevents the separation of the wind-driven surface currents from the geostrophic flow and the evaluation of the role of the frictional forcing induced by the wind alone on the current vorticity. High-resolution data of wind direction from HF radar provided insights on the wind spatial and temporal variability and the interaction between submesoscale fronts and wind. The development of the techniques for the extraction of wind speeds from HF radar measurements would provide valuable data for the understanding of the coastal dynamics at submesoscale.

References

Alpers, W., P. Brandt, A. Lazar, D. Dagorne, B. Sow, S. Faye, M. W. Hansen, A. Rubino, P. M. Poulain, and P. Brehmer (2013), A small-scale oceanic eddy off the coast of West Africa studied by multi-sensor satellite and surface drifter data, *Remote Sens. Environ.*, *129*, 132–143.

Ardhuin, F., L. Marié, N. Rascle, P. Forget, and A. Roland (2009), Observation and estimation of Lagrangian, Stokes, and Eulerian currents induced by wind and waves at the sea surface, *J. Phys. Oceanogr.*, *39*, 2820–2838.

Baird, M. E., I. M. Suthers, D. A. Griffin, B. Hollings, C. Pattiaratchi, J. D. Everett, M. Roughan, K. Oubelkheir, and M. Doblin (2011), The effect of surface flooding on the physical–biogeochemical dynamics of a warm-core eddy off southeast Australia, *Deep Sea Res., Part II*, *58*(5), 592–605.

Barth, J. A. (1989), Stability of a coastal upwelling front: 1. Model development and a stability theorem, *J. Geophys. Res.*, *94*(C8), 10,844–10,856.

Barth, J. A. (1994), Short-wave length instabilities on coastal jets and fronts, *J. Geophys. Res.*, *99*(C8), 16,095–16,115.

Bendat, J. S., and A. G. Piersol (2010), *Random Data, Analysis and Measurement Procedures*, John Wiley, New York, doi:10.1002/9781118032428.

Cenedese, C., R. E. Todd, G. G. Gawarkiewicz, W. B. Owens, and A. Y. Shcherbina (2013), Offshore transport of shelf waters through interaction of vortices with a shelf break current, *J. Phys. Oceanogr.*, *43*, 905–919.

Chang, Y.-C., G.-Y. Chen, R.-S. Tseng, L. R. Centurioni, and P. C. Chu (2012), Observed near-surface currents under high wind speeds, *J. Geophys. Res.*, *117*, C11026, doi:10.1029/2012JC007996.

Eldevik, T., and K. B. Dysthe (2002), Spiral eddies, *J. Phys. Oceanogr.*, *32*, 851–869.

Emery, W. J., and R. E. Thomson (2004), *Data Analysis Methods in Physical Oceanography*, 2nd ed., chap. 5, pp. 371–564, Elsevier, Sydney, N. S. W., Australia.

Everett, J. D., M. E. Baird, and I. M. Suthers (2011), Three-dimensional structure of a swarm of the salp Thalia democratica within a cold-core eddy off southeast Australia, *J. Geophys. Res.*, *116*, C12046, doi:10.1029/2011JC007310.

Everett, J. D., H. MacDonald, M. E. Baird, J. Humphries, M. Roughan, and I. M. Suthers (2015), Cyclonic entrainment of preconditioned shelf waters into a frontal eddy, *J. Geophys. Res. Oceans*, *120*, 677–691, doi:10.1002/2014JC010301.

Ferrari, R. (2011), A frontal challenge for climate models, *Science*, *332*, 316–317.

Graber, H. C., B. K. Haus, R. D. Chapman, and L. K. Shay (1997), HF radar comparisons with moored estimates of current speed and direction: Expected differences and implications, *J. Geophys. Res.*, *102*(C8), 18,749–18,766.

Gruber, N., Z. Lachkar, H. Frenzel, P. Marchesiello, M. Münnich, J. C. McWilliams, T. Nagai, and G. K. Plattner (2011), Eddy-induced reduction of biological production in eastern boundary upwelling systems, *Nat. Geosci.*, *4*, 787–792.

Gula, J., M. J. Molemaker, and J. C. McWilliams (2015), Submesoscale cold filaments in the Gulf Stream, *J. Phys. Oceanogr.*, *44*, 2617–2643.

Hansen, C., E. Kvaleberg, and A. Samuelsen (2010), Anticyclonic eddies in the Norwegian Sea: Their generation, evolution and impact on primary production, *Deep Sea Res., Part I*, 57(9), 1079–1091.

Haza, A. C., T. M. Özgökmen, A. Griffa, A. Molcard, P.-M. Poulain, and G. Peggion (2010), Transport properties in small-scale coastal flows: relative dispersion from VHF radar measurements in the Gulf of La Spezia, *Ocean Dyn.*, 60, 861–882.

Kaplan, D. M., and J. Largier (2006), HF radar-derived origin and destination of surface waters off Bodega Bay, California, *Deep Sea Res., Part II*, 53, 2906–2930.

Klocker, A., R. Ferrari, J. H. Lacasce, and S. T. Merrifield (2012), Reconciling float-based and tracer-based estimates of lateral diffusivities, *J. Mar. Res.*, 70(4), 569–602.

Largier, J. L. (2003), Considerations in estimating larval dispersal distances from oceanographic data, *Ecol. Appl.*, 13(1), S71–S89.

Lekien, F., C. Coulliette, A. J. Mariano, E. H. Ryan, L. K. Shay, G. Haller, and J. Marsden (2005), Pollution release tied to invariant manifolds: A case study for the coast of Florida, *Physica D*, 210, 1–20.

Lévy, M., R. Ferrari, P. J. S. Franks, A. P. Martin, and P. Rivière (2012), Bringing physics to life at the submesoscale, *Geophys. Res. Lett.*, 39, L14602, doi:10.1029/2012GL052756.

Lilly, J. M. (2016), *jLab: A Data Analysis Package for Matlab*, v. 1.6.2. [Available at http://www.jmlilly.net/jmlsoft.html.]

Lozier, M. S., and M. S. C. Reed (2005), The influence of topography on the stability of shelf break fronts, *J. Phys. Oceanogr.*, 35, 1023–1036.

Lozier, M. S., M. S. C. Reed, and G. G. Gawarkiewicz (2002), Instability of a shelf break front, *J. Phys. Oceanogr.*, 32, 924–944.

Macdonald, H. S., M. Roughan, M. E. Baird, and J. Wilkin (2013), A numerical modeling study of the East Australian Current encircling and overwashing a warm-core eddy, *J. Geophys. Res. Oceans*, 118, 301–315, doi:10.1029/2012JC008386.

Mahadevan, A., and A. Tandon (2006), An analysis of mechanisms for submesoscale vertical motion at ocean fronts, *Ocean Model.*, 14, 241–256.

Mantovanelli, A., and M. L. Heron (2012), Radar-based tracking of pollutants/larvae in the Coral Sea, paper presented at the 12th International Coral Reef Symposium, Cairns, Queensland, Australia, 9–13 July, Authors Sponsored by Queensland Department of Tourism, Regional Development and Industry and James Cook University.

Mantovanelli, A., M. L. Heron, A. Prytz, C. R. Steinberg, and D. Wisdom (2011), Validation of radar-based Lagrangian trajectories against surface-drogued drifters in the Coral Sea, Australia, in *IEEE Oceans 2011*, pp. 1–4, IEEE, Waikoloa, Hawaii, doi:10.23919/OCEANS.2011.6107233.

Mantovanelli, A., M. L. Heron, S. F. Heron, and C. R. Steinberg (2012), Relative dispersion of surface drifters in a barrier reef region, *J. Geophys. Res.*, 117, C11016, doi:10.1029/2012JC008106.

Mata, M. M., M. Tomczak, S. Wijffels, and J. A. Church (2000), East Australian Current volume transports at 30°S: Estimates from the World Ocean Circulation Experiment hydrographic sections PR11/P6 and the PCM3 current meter array, *J. Geophys. Res.*, 105(C12), 28,509–28,526.

Middleton, J. H., D. R. Cox, and P. M. Tate (1997), The oceanography of the Sydney region, *Mar. Pollut. Bull.*, 33(7-12), 124–131.

Mullaney, T. J., and I. M. Suthers (2013), Entrainment and retention of the coastal larval fish assemblage by a short-lived submesoscale, frontal eddy of the East Australian Current, *Limnol. Oceanogr.*, 58(5), 1546–1556.

Munk, W., L. Armi, K. Fischer, and F. Zachariasen (2000), Spirals on the sea, *Proc. R. Soc. London, Ser. A.*, 456, 1217–1280.

Nencioli, F., F. d' Ovidio, A. M. Doglioli, and A. Petrenko (2013), In situ estimates of submesoscale horizontal eddy diffusivity across an ocean front, *J. Geophys. Res. Oceans*, 118, 7066–7080, doi:10.1002/2013JC009252.

Owen, R. W. (1981), Fronts and eddies in the sea: mechanisms, interaction and biological effects, in *Analysis of Marine Ecosystems*, edited by A. R. Longhurst, pp. 197–233, Academic, London.

Parks, A. B., L. K. Shay, W. E. Johns, J. Martinez-Pedraja, and K. W. Gurgel (2009), HF radar observations of small-scale surface current variability in the Straits of Florida, *J. Geophys. Res.*, 114, C08002, doi:10.1029/2008JC005025.

Pasquet, A., T. Szekely, and Y. Morel (2012), Production and dispersion of mixed waters in stratified coastal areas, *Cont. Shelf Res.*, 39–40, 49–77.

Poulain, P.-M., A. Bussani, R. Gerin, R. Jungwirth, E. Mauri, M. Menna, and G. Notarstefano (2013), Mediterranean surface currents measured with drifters: From basin to sub-inertial scales, *Oceanography*, 26(1), 38–47.

Rio, M.-H., and F. Hernandez (2003), High-frequency response of wind-driven currents measured by drifting buoys and altimetry over the world ocean, *J. Geophys. Res.*, 108(C8), 3283, doi:10.1029/2002JC001655.

Rossi, V., A. Schaeffer, J. Wood, G. Galibert, B. Morris, J. Sudre, M. Roughan, and A. M. Waite (2014), Seasonality of sporadic physical processes driving temperature and nutrient high-frequency variability in the coastal ocean off southeast Australia, *J. Geophys. Res. Oceans*, 119, 1–16, doi:10.1002/2013JC009284.

Roughan, M., E. J. Terrill, J. L. Largier, and M. Otero (2005), Observations of divergence and upwelling around Point Loma, California, *J. Geophys. Res.*, 110, C04011, doi:10.1029/2004JC002662.

Roughan, M., H. S. Macdonald, M. E. Baird, and T. M. Glasby (2011), Modelling seasonal and interannual variability in a Western Boundary Current and its impact on coastal connectivity, *Deep Sea Res., Part II*, 58(5), 628–644.

Roughan, M., S. R. Keating, A. Schaeffer, P. Cetina Heredia, C. Rocha, D. Griffin, R. Robertson and I. M. Suthers (2017), A tale of two eddies: The bio-physical characteristics of two contrasting cyclonic eddies inthe East Australian Current System, *J. Geophys. Res: Oceans*, doi: 10.1002/2016JC012241, in press.

Savitzky, A., and M. J. E. Golay (1964), Smoothing and differentiation of data by simplified least squares procedures, *Anal. Chem.*, 36(8), 1627–1639.

Schaeffer, A., A. Molcard, P. Forget, P. Fraunie, and P. Garreau (2011), Generation mechanism of mesoscale eddy in the Gulf of Lions: Radar observation and modelling, *Ocean Dyn.*, 61(10), 1587–1609.

Schaeffer, A., M. Roughan, and B. D. Morris (2013), Cross-shelf dynamics in a western boundary current regime: Implications for upwelling, *J. Phys. Oceanogr.*, 43, 1042–1059.

Schaeffer, A., M. Roughan, and B. D. Morris (2014a), CORRIGENDUM, *J. Phys. Oceanogr.*, 44, 2812–2813.

Schaeffer, A., M. Roughan, and J. E. Wood (2014b), Observed bottom boundary layer transport and uplift on the continental shelf adjacent to a western boundary current, *J. Geophys. Res. Oceans*, 119, 4922–4939, doi:10.1002/2013JC009735.

Schaeffer, A., A. Gramoulle, M. Roughan and A. Mantovanelli (2017), Characterizing frontal eddies along the East Australian Current from HF radar observations, *J. Geophys. Res.: Oceans*, doi:10.1002/2016JC012171, in press.

Thomas, L. N., and C. M. Lee (2005), Intensification of ocean fronts by down-front winds, *J. Phys. Oceanogr.*, 35, 1086–1102.

Thomas, L. N., A. Tandon, and A. Mahadevan (2008), Submesoscale processes and dynamics, in *Ocean Modelling in an Eddying Regime, Geophys. Monogr. Ser.*, vol. 177, edited by M. W. Hecht and H. Hasumi, pp. 17–37, AGU, Washington, D. C.

Tokeshi, R., K. Ichikawa, S. Fujii, K. Sato, and S. Kojima (2007), Estimating the geostrophic velocity obtained by HF radar observations in the upstream area of the Kuroshio, *J. Oceanogr.*, 63, 711–720.

Williams, R. G., and M. J. Follows (2011), *Ocean Dynamics and the Carbon Cycle: Principles and Mechanisms*, 416 pp., Cambridge Univ. Press, Cambridge, U. K.

Witter, D. L., and D. B. Chelton (1998), Eddy–mean flow interaction in zonal oceanic jet flow along zonal ridge topography, *J. Phys. Oceanogr.*, *28*, 2019–2039.

Wyatt, L. R. (2012), Shortwave direction and spreading measured with HF radar, *J. Atmos. Oceanic Technol.*, *29*, 286–299.

Wyatt, L. R., L. J. Ledgard, and C. W. Anderson (1997), Maximum likelihood estimation of the directional distribution of 0.53Hz ocean waves, *J. Atmos. Oceanic Technol.*, *14*, 591–603.

Wyatt, L. R., A. Mantovanelli, M. L. Heron, M. Roughan, and C. R. Steinberg (2017), *Assessment of Surface Currents Measured With High-Frequency Phased-Array Radars in Two Regions of Complex Circulation*, IEEE Oceanic Eng. Soc., doi:10.1109/JOE.2017.2704165, in press.